April 16, 2004

The Micro-Pulse Lidar Network (MPLNET): a federated network of micro-pulse lidars and AERONET sunphotometers

Authors:
Ellsworth J. Welton*, James R. Campbell, James D. Spinhirne,
Timothy A. Berkoff, Brent Holben, and Si-Chee Tsay

We present the formation of a new global-ground based eye-safe lidar network, the NASA Micro-Pulse Lidar Network (MPLNET). The aim of MPLNET is to acquire long-term observations of aerosol and cloud vertical profiles at unique geographic sites within the NASA Aerosol Robotic Network (AERONET). MPLNET utilizes standard instrumentation and data processing algorithms for efficient network operations and direct comparison of data between each site. The micro-pulse lidar is eye-safe, compact, and commercially available, and most easily allows growth of the network without sacrificing standardized instrumentation goals. Network growth follows a federated approach, pioneered by AERONET, wherein independent research groups may join MPLNET with their own instrument and site. MPLNET sites produce not only vertical profile data, but also column-averaged products already available from AERONET (aerosol optical depth, sky radiance, size distributions). Algorithms are presented for each MPLNET data product. Real-time Level 1 data products (next-day) include daily lidar signal images from the surface to ~20km, and Level 1.5 aerosol extinction profiles at times co-incident with AERONET observations. Quality assured Level 2 aerosol extinction profiles are generated after screening the Level 1.5 results and removing bad data. Level 3 products include continuous day/night aerosol extinction profiles, and are produced using Level 2 calibration data. Rigorous uncertainty calculations are presented for all data products. Analysis of MPLNET data show the MPL and our analysis routines are capable of successfully retrieving aerosol profiles, with the strenuous accounting of uncertainty necessary for accurate interpretation of the results.

* Lead Author: Dr. E. J. Welton
                  NASA GSFC Code 912
                  Ellsworth.J.Welton@nasa.gov

The Micro-pulse Lidar Network (MPLNET): a federated network of micro-pulse lidars and AERONET sunphotometers

Submission to the Journal of Atmospheric and Oceanic Technology

Ellsworth J. Welton[1], James R. Campbell[2], James D. Spinhirne[2], Timothy A. Berkoff[4], Brent Holben[4], and Si-Chee Tsay[5]

1. NASA Goddard Space Flight Center, Code 912
    Greenbelt, Maryland, 20771 USA

2. Science Systems and Applications, Inc.
    Lanham, Maryland, 20706 USA

3. Goddard Earth Sciences and Technology Center
    University of Maryland Baltimore County
    Baltimore, Maryland, 21250 USA

4. NASA Goddard Space Flight Center, Code 923
    Greenbelt, Maryland, 20771 USA

5. NASA Goddard Space Flight Center, Code 913
    Greenbelt, Maryland, 20771 USA

Draft Version: Ellsworth Welton, 4/16/04

Abstract

We present the formation of a new global-ground based eye-safe lidar network, the NASA Micro-Pulse Lidar Network (MPLNET). The aim of MPLNET is to acquire long-term observations of aerosol and cloud vertical profiles at unique geographic sites within the NASA Aerosol Robotic Network (AERONET). MPLNET utilizes standard instrumentation and data processing algorithms for efficient network operations and direct comparison of data between each site. The micro-pulse lidar is eye-safe, compact, and commercially available, and most easily allows growth of the network without sacrificing standardized instrumentation goals. Network growth follows a federated approach, pioneered by AERONET, wherein independent research groups may join MPLNET with their own instrument and site. MPLNET sites produce not only vertical profile data, but also column-averaged products already available from AERONET (aerosol optical depth, sky radiance, size distributions). Algorithms are presented for each MPLNET data product. Real-time Level 1 data products (next-day) include daily lidar signal images from the surface to ~20km, and Level 1.5 aerosol extinction profiles at times co-incident with AERONET observations. Quality assured Level 2 aerosol extinction profiles are generated after screening the Level 1.5 results and removing bad data. Level 3 products include continuous day/night aerosol extinction profiles, and are produced using Level 2 calibration data. Rigorous uncertainty calculations are presented for all data products. Analysis of MPLNET data show the MPL and our analysis routines are capable of successfully retrieving aerosol profiles, with the strenuous accounting of uncertainty necessary for accurate interpretation of the results.

1. Introduction

The state of the earth system has become an increasingly important subject over the past several decades, particularly the last few years. Of primary importance is to determine to what degree human activity causes changes in the earth's climate, as well as what portion is due to nature alone. Many factors contribute to the state of the climate. One major contribution is the manner in which the earth system interacts with solar radiation. Atmospheric gases, clouds, aerosols (suspended particles in the atmosphere such as dust and pollution), oceans, land surfaces, plants, animals, and humans all interact with this radiation and the net effect leads to the evolution of the climate. As the initial interaction with the incoming solar radiation occurs in the atmosphere, this region is of particular importance. While the impact of atmospheric gases on the climate has received much attention over the years, until recent years there was less focus directed toward studying the impacts from aerosols and clouds. Some of the recent aerosol related experiments include the Tropospheric Aerosol Radiative Forcing Observational Experiment (TARFOX) (Russell et al. 1999), the Aerosol Characterization Experiment 2 (ACE-2) (Raes et al. 2000), the Indian Ocean Experiment (INDOEX) (Ramanathan et al. 2001), and the Aerosol Characterization Experiment – Asia (ACE-Asia) (Huebert et al. 2003). Results from these and similar experiments have indicated that the radiative impacts from aerosols and clouds can be equal to or greater then that from greenhouse gases, particularly on a regional scale.

The Third Assessment Report of the Intergovernmental Panel on Climate Change (IPCC) states that atmospheric measurements of aerosols have lagged behind the growth in knowledge of their importance in the climate (Houghton et al. 2001). Aerosols directly effect the balance of solar radiation in the atmosphere by scattering and absorbing sunlight, thereby warming or cooling different parts of the atmosphere relative to one another. They also alter the amount of radiation that reaches the earth's surface, and that the surface in turn emits back towards space. Aerosols also indirectly effect the climate through their interaction with clouds, which in turn changes their physical and optical properties. The properties of clouds determine how they precipitate, which impacts other segments of the earth's climate as well as human activity. Aerosols also impact other areas not directly associated with the climate because they effect air quality. Aerosols can pose health risks because substantial portions of them are sub-micron in size and are small enough to enter the lungs (Pope et al. 2002). They also directly effect visibility and impact the overall quality of living humans in the surrounding area encounter. The reduction in visibility can also cause a hazard to both air and ground traffic that must pass through thick aerosol plumes such as dust storms and smoke from forest and brush fires.

Measuring the physical and optical properties of aerosols is difficult because they each derive from a variety of sources or mechanisms, have a wide spectrum of particle sizes, and there is a large spatial and temporal variability in their concentrations and composition. Traditionally, intensive field campaigns have been performed over short time periods to study a specific aspect of aerosols. While these types of experiments yield much in the way of determining key aerosol properties, they are confined in both time and space. It is much more difficult to perform the same type of observations from a global, or even regional, perspective because a large portion of the earth must be observed for long time periods. There are now many globally oriented aerosol measurements available from both ground and space-based platforms, for brevity we mention only a few. The NASA Aerosol Robotic Network (AERONET) operates automated sunphotometers from ground-based sites to acquire information on the optical and physical properties of aerosols (Holben et al. 1998). The NASA Moderate Resolution Imaging Spectro-

radiometer (MODIS) onboard the TERRA spacecraft has a wide range of wavelengths, and is capable of studying both aerosols and clouds (King et al. 2003). The NASA Total Ozone Mapping Spectrometer (TOMS) has demonstrated the ability to measure both atmospheric gases, as well as aerosols, from space (Herman et al. 1997). These efforts use passive remote sensing techniques that analyze the atmospheric column as a whole and can not directly determine aerosol vertical profiles. The NASA/NASDA Tropical Rainfall Measuring Mission (TRMM) is aimed primarily at studying clouds, particularly with regard to precipitation, using a variety of different sensors on the spacecraft (Kummerow et al. 2000). TRMM and ground-based weather services utilize radar to profile the vertical distribution of clouds and precipitation but these measurements do not yield information about aerosol profiles.

Aerosol vertical distribution is an important parameter because the height of aerosol layers determines where in the atmosphere scattering and absorption of sunlight occurs. This is especially true for absorbing aerosols that can alter the heating rate profile. In addition, aerosols and clouds must be at the same altitudes for the indirect effect to occur, such knowledge is difficult to obtain from passive sensors. Finally, the injection height of aerosols from their sources is connected to their production process, such as the connection between the heat from forest fires and smoke plume injection heights (Lavoué et al. 2000). Studies of aerosol transport processes between sources and downwind locations require accurate height profile information.

One instrument capable of providing vertical profiles of aerosol and cloud structure is a backscatter lidar (henceforth referred to simply as lidar). Lidars determine the range of aerosols and clouds by firing a short pulse of laser light and then measuring the time-of-flight from pulse transmission to reception of a returned signal. The returned signal is a function of time, converted into range using the speed of light, and is proportional to the amount of light backscattered by atmospheric molecules (Rayleigh scattering), aerosols, and clouds. Long established techniques exist to analyze lidar signals and produce not only layer heights, but also extinction profiles and optical depth information for transmissive layers (Fernald et al. 1972; Klett 1981). Lidars can be used to study all but the very thickest of aerosol layers. Lidars generally cannot penetrate thick clouds, and are usually used only to provide base height information. However, thin clouds, such as cirrus, can often be studied as effectively as aerosols. Here we focus on using lidars to study aerosol layers, but also to provide an indication of the presence of clouds at an altitude that could lead to studying aerosol-cloud interactions and the indirect effect.

Space-based lidar measurements are most desirable for long-term global studies. In January 2003, NASA launched the Geoscience Laser Altimeter System (GLAS) onboard the ICESat spacecraft. GLAS is an altimeter and a two-wavelength backscatter lidar that obtains global aerosol profiles (Zwally et al. 2002). NASA will launch another space-based two-wavelength backscatter lidar in 2005, the Cloud-Aerosol Lidar and Infared Pathfinder Satellite Observations (CALIPSO) (Winker et al. 2002). Both of these missions provide key measurements of global aerosol vertical distribution. However, joint observations of aerosol properties from space as well as from ground-based networks have been shown to provide the most accurate and informative data (Kaufman et al. 2002). This is due to the aerosol's spatial and temporal variations in composition and concentration, and also because the satellite measurements require routine validation from ground-based observations. Furthermore, the algorithms used to analyze the satellite aerosol data often require lookup tables of key parameters, and ground-based data is often needed to construct the table. The IPCC 2001 report discusses the need for the development and support of systematic ground-based measurements,

and in particular, the desire for a dramatic increase in systematic vertical profile measurements. The objective of this paper is to present a ground-based network capable of providing long-term, systematic aerosol profiles on time and spatial scales of use not only to case and regional studies, but global applications as well.

Two ground-based lidar networks, the Asian Dust Network (AD-Net) (Murayama et al. 2001) and the European Aerosol Research Lidar Network (EARLINET) (Bösenberg et al. 2001) provide routine aerosol and cloud profiling, but their observations are limited to the Asian and European regions, respectively. In addition, the Atmospheric Radiation Measurement (ARM) Program (Stokes and Schwartz 1994) operates lidars at their Cloud and Radiation Testbed (CART) sites, however there are only four of them. Data from each of these networks is certainly of immense value, however one would have to gather each of the separate data sets and merge them together before beginning any sort of global study. As these networks contain a wide array of different lidar systems, operating protocols, and data processing techniques, this task could become quite time consuming. Furthermore, many of the lidars in these networks are not well suited for long-term deployments in remote areas; therefore it would be difficult to expand their observations globally.

The formation of a new ground-based lidar network is desired. The primary focus of the new network is to provide continuous, long-term observations of both aerosol and cloud vertical distribution using sites located throughout the world. In order to provide continuous, long-term measurements in possibly remote areas, the lidar system must be able to operate for long periods unattended. This requires a small, rugged, and eye-safe lidar. The cost and availability of the lidar is also important because many of them are required. In order to overcome difficulties associated with merging different data sets, it is best to use only one lidar system and common, standardized data processing algorithms. Such a network would fulfill the demand stated in the IPCC 2001 report, and also address problematic issues encountered by the other lidar networks.

The Micro-pulse Lidar (MPL) was developed by the Cloud and Aerosol Lidar Group at NASA Goddard Space Flight Center (GSFC) in the early 1990s (Spinhirne et al. 1995). The MPL is the most desirable instrument for the new network because it operates autonomously, is eye-safe, and is commercially available. The MPL has been deployed in support of numerous field experiments and has demonstrated the ability to measure aerosol properties in nearly every major aerosol campaign since ACE-2. Data processing algorithms were developed to analyze MPL data from each of the field experiments and ARM sites. The older processing algorithms can be modified to process data for each site in the new network. The necessary modifications include the rigorous determination of uncertainties for all data products, and the ability to use common, standardized algorithms to automatically process large portions of MPL data from a variety of locations.

This paper presents the formulation of a new globally based lidar network using MPL systems. The new network is called MPLNET. Here we present the structure of the network, including site locations, deployment strategies, and instrumentation issues. Data processing algorithms are also presented, along with a description of several data products and their bias errors and computational limitations. Initial results from MPLNET measurements are shown to provide an indication of the utility of a network of this type.

2. The Micro-pulse Lidar System Description

The MPL is a compact and eye-safe lidar system capable of determining the range of aerosols and clouds by firing a short pulse of laser light (at 523 nm) and measuring the time-of-flight from pulse transmission to reception of a returned signal. The returned signal is a function of time, converted into range using the speed of light, and is proportional to the amount of light backscattered by atmospheric molecules (Rayleigh scattering), aerosols, and clouds. The evolution of the MPL from the initial Spinhirne et al. (1995) optical design to the type now used in MPLNET is described in detail by Campbell et al. (2002), including on-site maintenance, and calibration techniques. Here we provide only an overview of the basic characteristics of the MPL.

The MPL achieves ANSI eye-safe standards by using low output energies (μJ), and beam expansion to ~20 cm in diameter. The MPL laser pulse duration is 10 ns with a pulse repetition frequency (PRF) of 2500 Hz and output energies range from 1 to 10 μJ depending upon system performance and operational settings. The high PRF allows the system to average many low energy pulses in a short time to achieve a good signal-to-noise ratio. The MPL transmitter-receiver consists of either a 20.32 cm or 17.77 cm diameter Cassegrain telescope with optics and electronics mounted directly below the telescope. The laser supply and scalar (data binning unit) are connected to the transmitter-receiver, along with a control computer. The MPL must be operated inside a climate-controlled housing. The laser system contains a diode pumped Nd:YLF laser with a fundamental pulse output wavelength of 1046 nm that is converted to 523 nm after passage through a frequency doubling crystal just prior to transmission by the telescope. Signals are received using the same telescope and are recorded with a Geiger mode avalanche photodiode. Detector quantum efficiencies range from 40% in older models to 50% in currently available detectors (Valencia et al. 2004). Receiver optical transmission efficiencies range from ~1% to ~12% (Currie et al. 2004) depending upon the condition of the individual components, especially the dual 523 nm filters. Signals and associated instrument readings are stored in binary data files on the control computer. MPLNET instruments store data at either 30 seconds or 1-minute time resolution, and either 30 or 75-meter vertical resolution.

3. The Micro-pulse Lidar Network (MPLNET)

The Micro-pulse Lidar Network (MPLNET) was proposed in 1999, and began operation in the summer of 2000 using funding provided by the NASA Earth Observing System (EOS). The initial strategy was to create new MPLNET NASA funded sites and to form partnerships with other groups in possession of an MPL. Figure 1 shows the locations of the first two NASA sites at the South Pole and GSFC. MPLNET sites are also co-located with AERONET sunphotometers because the MPL data processing routines are based on an algorithm that requires an independent measurement of aerosol optical depth (Welton et al. 2000). The joint MPLNET/AERONET sites are essentially super-sites that measure aerosol vertical structure, cloud presence, aerosol column optical depth and size distribution, and sky radiance. Polar sites shown in Figure 1 are not co-located with AERONET because they are used primarily for cloud and snow studies.

In order to build upon the initial MPL sites, the MPLNET project was designed to use a federated system of sites similar to that already employed by the AERONET project. In this system, independent research groups owning MPL systems can propose to join MPLNET and setup their own site. This arrangement reduces the burden on the MPLNET project to acquire funding to purchase or build new MPL systems, and also serves to incorporate otherwise

separate groups into a larger research effort. The MPLNET project performs all instrument maintenance and repair, ensuring that the instruments are in peak condition and the data quality is high. The MPLNET project also performs all data processing and archiving using data processing algorithms discussed in Section 4.

Figure 1 shows MPLNET sites established after the initial sites, as well as proposed locations, and is current as of the date of this publication. The NASA CERES Ground Validation Group supplied four MPL systems to the project, and the NASA TOMS group contributed their MPL for field experiments. These other NASA instruments will soon be deployed to the proposed sites shown in Figure 1. Also, the National Institute of Polar Research (NIPR) in Japan is now operating two sites, and a group at the Marine Meteorology Division at the Naval Research Labs Monterey will soon have a new site. Several other research groups have expressed interest in joining the network using their own instruments, and new sites are forthcoming. Additional funding is now provided from the NASA Radiation Sciences Program to accommodate the growth of the network.

In addition to the long-term network sites, a number of field experiments are conducted each year, usually as part of larger multinational field campaigns. Also, the NASA Sensor Intercomparison and Merger for Biological and Interdisciplinary Oceanic Studies (SIMBIOS) project has provided funds to deploy an MPL during research cruises in support of ocean color validation. The field experiments provide a connection between the long-term globally focused studies and regional and case studies performed in the experiments. In addition, they often provide the means to initiate a new long-term site at a remote location. All together, the MPLNET project has participated in four major field experiments since 2000. Figure 1 also shows the locations of field experiments and cruises. During 2000, an MPL was deployed in support of the Puerto Rico Dust Experiment (PRIDE), and two MPL systems were operated in Southern Africa during the Southern African Regional Science Initiative (SAFARI). In 2001, MPL systems were deployed to China and onboard a research vessel off the coast of Asia during ACE-Asia. Finally, MPL systems were operated during the Chesapeake Lighthouse and Aircraft Measurements for Satellites (CLAMS) campaign in 2001, and the Cirrus Regional Study of Tropical Anvils and Cirrus Layers -- Florida Area Cirrus Experiment (CRYSTAL-FACE) in 2002.

4. MPLNET Data Products and Processing Techniques

A list of current MPLNET data products is shown in Table 1. This section describes the techniques used to process raw MPL data into these data products. Level 1, 1.5, 2, and 3 processing algorithms are presented. The level 1 algorithm has been previously published, but we present the basic equations and information here in order to provide a foundation from which to present the remaining algorithms.

4.1 Level 1 Data Products

Following Campbell et al. 2002, the measured MPL signal can be written as,

---

$$P_{raw}(r) = \frac{CEO(r)[\beta_M(r)+\beta_P(r)]T_M^2(r)T_P^2(r)T_O^2(r)}{D(P_{raw})r^2} + \frac{A_{raw}(r,E)}{D(P_{raw})} + \frac{B_{raw}}{D(P_{raw})} \qquad (1)$$

where $P_{raw}(r)$ is the measured signal (counts/bin) at range bin r (km) from the lidar. E is the output laser pulse energy (μJ). B is the solar background signal and also includes dark noise in the detector (usually small compared to the background).

$D(P_{raw})$ is the detector dead-time factor. Dead-time effects are caused by saturation of the detector signals at high-count rates, and are corrected for by dividing the measured signal by $D(P_{raw})$. The dead-time factor is determined during a calibration procedure, and the uncertainty in the dead-time correction is assumed to be small (Welton and Campbell 2002).

The two instrument parameters, $A_{raw}(r,E)$ and $O(r)$, are not significant for all lidars but are very important for the MPL. $A_{raw}(r,E)$ is termed afterpulse, and accounts for any signal induced noise from the initial laser flash. $O(r)$ is termed overlap, and accounts for signal loss in the near-range due to poor receiver efficiency of the telescope and associated optics at close range.

The backscatter cross-sections, $\beta_M(r)$ and $\beta_P(r)$, are due to molecules and particles, respectively. The particles are either from clouds, aerosols, or both. The backscatter cross-sections are in units of km⁻¹sr⁻¹. The transmission terms, $T_M^2(r)$, $T_P^2(r)$, and $T_O^2(r)$ are given by the following

$$T_i^2(r) = \exp\left[-2\int_{r_L} \sigma_i(r')dr'\right] \qquad (2)$$

where the i subscript denotes either a molecular, particle, or ozone quantity, and r_L is the lidar altitude. $\sigma(r)$ is the extinction coefficient in units of km⁻¹, and is due to both scattering and absorption (only absorption for ozone). The integral of the extinction coefficient from the lidar to any range is the optical depth, τ, over that distance. The transmission terms are squared to account for the two-way path of the laser pulses.

C_s is the MPL system calibration value and is given as

$$C = \left[\frac{A\lambda q T_R}{2h}\right]T_W \qquad (3)$$

where A is the area of the receiver, λ is the wavelength, q is the quantum efficiency of the detector, T_R is the transmission efficiency of the receiver, h is the Plank constant. The MPL systems are enclosed inside a climate controlled box or laboratory and data is taken through a window. T_W is the efficiency of the window. Theoretical values of C, without a window, have been calculated using the values of the Eq. (3) parameters given in Section 2. Values of C range from ~45 to ~700 (km³)/(μJ•μsec) for MPL systems with the 20.32 cm telescope, and ~30 to ~500 (km³)/(μJ•μsec) with the 17.77 cm telescope. These theoretical values serve only as a guideline because T_R and q vary slightly for each MPL system. In fact, low values of C are often an indication of poor filters or some other optical aberration.

The important terms in the raw data are those parameters due only to signal returns from the atmosphere. Therefore, the first step is to reduce the raw data to a form that is dependent upon a minimum of instrument parameters. Campbell et al. (2002) describe procedures for

converting raw MPL data to a form which is dependent upon only one instrument parameter, C, and that is proportional to the backscatter and transmission terms in the atmosphere. The converted signal is called the normalized-relative-backscatter signal, henceforth referred to as the NRB signal. The NRB signal, $P_{NRB}(r)$, is given by

$$P_{NRB}(r) = C[\beta_M(r) + \beta_P(r)]T_M^{-2}(r)T_P^{-2}(r)T_O^{-2}(r) \qquad (4)$$

with units of km²/(μJ•μsec). Welton and Campbell (2002) discuss the uncertainty in NRB signals, which is given by

$$\delta P_{NRB}(r) = P_{NRB}(r)\sqrt{\frac{\delta P(r)^2 + \delta B^2 + \delta A(r)^2}{[P(r) - B - A(r)]^2} + \left[\frac{\delta E}{E}\right]^2 + \left[\frac{\delta O(r)}{O(r)}\right]^2} \qquad (5)$$

where the subscript, *raw*, has been dropped from the P, A, and B parameters because they have been dead time corrected.

The level 1.0 NRB data products are produced in real-time, and daily browse images are available on the MPLNET web site immediately thereafter. The NRB signals are useful for determining qualitative structure of aerosols and clouds over the course of a day or longer time period. NRB signals do not directly provide quantitative aerosol and cloud information because of the dependence on C, and the fact that backscatter has not been separated from attenuation (caused by extinction).

4.2 Level 1.5 Data Products

Level 1.5 data products use the level 1.0 NRB signals to solve for quantitative aerosol and cloud products. Level 1.5 data are produced in real-time immediately following the analysis of the level 1.0 data. Level 1.5 products are not screened to remove bad results, and are not considered to be quality assured data.

The level 1.5 algorithm analyzes the level 1.0 NRB signals, using co-located aerosol optical depth (AOD) measurements from AERONET, to separate backscatter from attenuation and produce a profile of aerosol extinction. Level 1.5 AERONET AOD are used in this process. Typically a 20 or 30 minute time averaged NRB signal is used for this analysis in order to reduce the net uncertainty in the NRB. The level 1.5 data are available only at times centered on AERONET observations. For the remainder of this section (4.2.1) the term NRB is used to refer to the time averaged signal. A simple cloud screen is used to remove signals contaminated by clouds prior to the average (Campbell et al. 2003). Therefore, for level 1.5 processing all particle terms in the MPL signal are due only to aerosols.

The first step in this procedure is to calibrate the MPL (determine C). The parameters in the bracket on the RHS of Eq. (3) can be calculated once the lidar is constructed, and ideally T_W ~ 1. Therefore, it is possible to calculate C prior to deployment of the MPL. However, the act of deploying the lidar may cause the optics to change slightly (due to movement or temperature) and thereby alter T_r. Also, T_W often varies because the cleanliness of the window at the site changes as time goes on. For these reasons, the theoretical value of C (with $T_W = 1$) is often used only as a reference point and instead, C is calculated directly from the level 1.0 data. The actual values of C can be compared to the theoretical value in order to track the overall health of the

9

MPL and site. For instance, if either the window becomes very dirty or something adverse occurs within the MPL, C will be much lower than the theoretical value because the overall transmission will decrease.

C is calculated from the NRB signal using the following equation,

$$C(r) = \frac{P_{NRB}(r)}{T_P^2 \beta_M(r) \chi(r) T_M^{-2}(r) T_O^{-2}(r)} \qquad (6)$$

where $C(r)$ is the calculated calibration constant at range r. The particle transmission term, T_P^2, is calculated using the AOD from the AERONET sunphotometer and therefore does not change with altitude. $\chi(r)$ is the scattering ratio,

$$\chi(r) = \frac{\beta_M(r) + \beta_P(r)}{\beta_M(r)} \qquad (7)$$

and is close to 1 when the aerosol concentration at range r is low. The procedures used to determine the molecular and ozone quantities are discussed in Appendix A.

It is important to identify a suitable calibration zone to apply Eq. (6). The zone must be above all aerosol layers, therefore $\beta_P(r) = 0$. In addition, signal-to-noise levels in the zone should be high enough to produce reasonable values of C. A calibration zone selection algorithm is discussed in the appendix of Campbell et al. (2003), and is based on searching for a region with minimum values of $C(r)$. At ranges below the zone, $C(r)$ will be larger than the true value because T_P^2 will be lower than it should due to using a fixed AOD from the sunphotometer. Although aerosols could be present at the lower ranges and therefore $\chi(r)$ would be larger than 1, $P_{NRB}(r)$ would also be increased and offset any effect due to $\chi(r)$. Therefore, $C(r)$ will approach a minimum value when r is in the calibration zone. The initial minimum value identifies the bottom of the calibration zone, and also determines the top of the highest aerosol layer (one of the level 1.5 data products).

Values of $C(r)$ are calculated at ranges up to 1 km from the bottom of the calibration zone using Eq. (6). The uncertainty in $C(r)$, termed $\delta C(r)$, is given by

$$\left[\frac{\delta C(r)}{C(r)}\right]^2 = \left[\frac{\delta P_{NRB}(r)}{P_{NRB}(r)}\right]^2 - \left[\frac{\delta P_{NRB}(r)}{P_{NRB}(r)}\right]^2 + \left[\frac{\delta \chi(r)}{\chi(r)}\right]^2 + \left[\frac{\delta \beta_M(r)}{\beta_M(r)}\right]^2 + \left[\frac{\delta T_M^2(r)}{T_M^2(r)}\right]^2 + \left[\frac{\delta T_O^2(r)}{T_O^2(r)}\right]^2 + \left[\frac{\delta T_P^2}{T_P^2}\right]^2 \qquad (8)$$

$\delta \chi(r)$, δT_P^2, and the molecular and ozone uncertainty terms are discussed in Appendix A. As shown in the Appendix, $\delta \chi(r)/ \chi(r)$ can be replaced with χ_m-1, where χ_m is the minimum scattering ratio detection limit and is calculated from the NRB signal.

The calculated values of $C(r)$ in the calibration zone are averaged to produce a final value for C,

$$C = \frac{1}{N}\sum_{i=1}^{N} C(r_i) \qquad (9)$$

10

where N is the number of range bins in the calibration zone, and r_1 and r_2 are the bottom and top of the calibration zone, respectively. The uncertainty in the final value of C is

$$\delta C = \frac{1}{N}\sqrt{\sum_{i=r_1}^{r_2}(\delta C(r_i))^2}$$ (10)

Another method may be used to calculate C. This method integrates both the NRB signal and the combined backscatter and transmission terms over the calibration zone to calculate C,

$$C_2 = \frac{\int_{r_1}^{r_2} P_{NRB}(r')dr'}{\int_{r_1}^{r_2} T_P^2\beta_M(r')\chi(r')T_M^2(r')T_O^2(r')dr'}$$ (11)

Both methods were found to calculate C values and uncertainties within 1% of one another. We have chosen to use the first method (Eq. (6)) because the equation used to calculate C is the same as the one used to locate the calibration zone.

The NRB signals are calibrated by dividing them by C. The resulting signal is referred to as the attenuated backscatter signal, or AB signal. The AB signal, $P_{AB}(r)$, is

$$P_{AB}(r) = [\beta_M(r) + \beta_P(r)]T_M^2(r)T_P^2(r) .$$ (12)

with units of $(km\cdot sr)^{-1}$ and the uncertainty in $P_{AB}(r)$ is

$$\delta P_{AB}(r) = P_{AB}(r)\sqrt{\left[\frac{\delta P_{NRB}(r)}{P_{NRB}(r)}\right]^2 + \left[\frac{\delta C}{C}\right]^2}$$ (13)

After the signal is calibrated and the top of the highest aerosol layer is found, the remaining step of the level 1.5 algorithm is to perform an inversion of the signal to produce aerosol backscatter and extinction profiles, and to calculate the aerosol extinction-to-backscatter ratio.

Extinction and backscatter are related using the extinction-backscatter ratio (units of sr),

$$S_i(r) = \frac{\sigma_i(r)}{\beta_i(r)}$$ (14)

where $S_i(r)$ is the extinction-backscatter ratio, and the i subscript indicates a molecular or aerosol quantity (M or A subscript). The extinction-to-backscatter ratio is defined by the following equation,

$$S_i = \frac{4\pi}{\omega_o P_i(180)}$$ (15)

11

where ω_o is the single scatter albedo, and $P_i(180)$ is the phase function at 180° (normalized to 4π). S_M is a constant and is equal to $8\pi/3$. S_A is unknown but typically ranges in value from 10 to 100 sr (Spinhirne et al. 1980; Ackermann 1998; Welton et al. 2002).

The inversion itself is described in the Appendix of Welton et al. (2000). We present the basics of the algorithm here in order to provide the foundation to discuss the calculation of uncertainties for the backscatter and extinction profiles, and S_A. For level 1.5 processing S_A is assumed to be constant with respect to range from the ground to the aerosol top height. In reality, S_A could change depending upon changes in the single scatter albedo and phase function of the aerosols in the layers below. The implications of using a constant S_A value are further discussed in Section 5.

The backward-solution of the backscatter term in the lidar equation is presented in Fernald (1984),

$$\beta_P(z-1) = \frac{P_{AB}(z-1)\Psi(z-1,z)}{\frac{P_{AB}(z)}{\beta_P(z)+\beta_M(z)} + S_A[P_{AB}(z)+P_{AB}(z-1)\Psi(z-1,z)]\Delta z} - \beta_M(z-1)$$ (16)

where

$$\Psi(z-1,z) = \exp\left[(S_A - S_M)(\beta_M(z-1) + \beta_M(z))\Delta z\right]$$ (17)

and z is the altitude bin one step above the $z-1$ altitude bin, and Δz is the lidar range interval (distance between bins). Ozone is ignored in this solution (Appendix A). The solution has two unknown quantities, therefore an iterative procedure was developed based on work presented in Marenco et al. (1997). The iterative procedure uses the pre-determined τ_P (sunphotometer AOD) to solve for the β_P profile and to calculate the value of S_A for the layer.

The iteration begins by setting $\beta_P(z)$ equal to zero one altitude bin above the aerosol top height (referred to as z_T). For the first iteration, S_A is set equal to 1 and the uncertainty, δS_A, is also set equal to 1 (100% uncertainty). β_P is calculated one altitude step below z_T (referred to as $\beta_P(z-1)$) using the form of Eq. 16). This process is repeated downward through the layer, with $S_A = 1$ and $\beta_P(z)$ obtained from the previous step, until the value of β_P is calculated at the bottom altitude bin immediately above the ground (z_B). At this point, a backscatter profile has been calculated for the first iteration.

In order to solve for the uncertainty in the backscatter profile, Eq. (16) is rewritten in a simplified form as

$$\beta_P(z-1) = \frac{X}{Y} - \beta_M(z-1)$$ (18)

where

$$X = P_{AB}(z-1)\Psi(z-1,z)$$ (19)

and

12

$$Y = \frac{P_{AB}(z)}{\beta_P(z) + \beta_M(z)} + S_A[P_{AB}(z) + P_{AB}(z-1)\Psi(z-1,z)]\Delta z \quad (20)$$

The uncertainty in the backscatter is given by

$$\delta\beta_P(z-1) = \sqrt{\left(\frac{X}{Y}\right)^2\left[\left(\frac{\delta X}{X}\right)^2 + \left(\frac{\delta Y}{Y}\right)^2\right] + (\delta\beta_M(z-1))^2} \quad (21)$$

The $\delta\beta_M(z-1)$ term is known (Appendix A), therefore only the $(\delta X/X)^2$ and $(\delta Y/Y)^2$ terms must be determined. The first step in this process is to solve for the $(\delta\Psi/\Psi)^2$ term, which is given by

$$\left(\frac{\delta\Psi}{\Psi}\right)^2 = [(S_A - S_M)(\beta_M(z-1) + \beta_M(z))\Delta z]^2\left[\left(\frac{\delta S_A}{S_A - S_M}\right)^2 + \frac{(\delta\beta_M(z-1))^2 + (\delta\beta_M(z))^2}{(\beta_M(z-1) + \beta_M(z))^2}\right] \quad (22)$$

The $(\delta X/X)^2$ term in Eq. (46) is then given by

$$\left(\frac{\delta X}{X}\right)^2 = \left(\frac{\delta P_{AB}(z-1)}{P_{AB}(z-1)}\right)^2 + \left(\frac{\delta\Psi}{\Psi}\right)^2 \quad (23)$$

The $(\delta Y/Y)^2$ term is more complicated and Y, Eq. (20), must first be rewritten as

$$Y = \eta + \phi \quad (24)$$

where

$$\eta = \frac{P_{AB}(z)}{\beta_P(z) + \beta_M(z)} \quad (25)$$

and

$$\phi = S_A[P_{AB}(z) + P_{AB}(z-1)\Psi(z-1,z)]\Delta z \quad (26)$$

The $(\delta Y/Y)^2$ term is then given by

$$\left(\frac{\delta Y}{Y}\right)^2 = \frac{(\delta\eta)^2 + (\delta\phi)^2}{Y^2} \quad (27)$$

The $(\delta\eta)^2$ and $(\delta\phi)^2$ terms are written as

13

$$(\delta\eta)^2 = \left(\frac{P_{AB}(z)}{\beta_P(z) + \beta_M(z)}\right)^2\left[\left(\frac{\delta P_{AB}(z)}{P_{AB}(z)}\right)^2 + \frac{(\delta\beta_P(z))^2 + (\delta\beta_M(z))^2}{(\beta_P(z) + \beta_M(z))^2}\right] \quad (28)$$

and

$$(\delta\phi)^2 = [S_A(P_{AB}(z) + P_{AB}(z-1)\Psi(z-1,z))\Delta z]^2\left[\left(\frac{\delta S_A}{S_A}\right)^2 + \Omega\right] \quad (29)$$

where

$$\Omega = \frac{(\delta P_{AB}(z))^2 + \left[\left(\frac{\delta P_{AB}(z-1)}{P_{AB}(z-1)}\right)^2 + \left(\frac{\delta\Psi(z-1,z)}{\Psi(z-1,z)}\right)^2\right](P_{AB}(z-1)\Psi(z-1,z))^2}{P_{AB}(z) + P_{AB}(z-1)\Psi(z-1,z)} \quad (30)$$

The final uncertainty in the backscatter profile values is then given by Eq. (21), using Eq. (23) for the $(\delta X/X)^2$ term and Eq. (27) to Eq. (30) for the $(\delta Y/Y)^2$ term.

After the end of the first iteration, the estimate of S_A must be improved for the next iteration (determination of S_{new}). S_{new} is determined using the β_P profile calculated in the first iteration and the following equation,

$$S_{new} = \frac{\tau_P}{\int_{z_s}^{z_T}\beta_P(z')dz'} \quad (31)$$

where τ_P is the AOD from the AERONET sunphotometer. The uncertainty in S_{new} is given by

$$\delta S_{new} = S_{new}\sqrt{\left(\frac{\delta\tau_P}{\tau_P}\right)^2 + \frac{(\Delta z)^2\sum_{z_s}^{z_T}(\delta\beta_P(i))^2}{\left(\Delta z\sum_{z_s}^{z_T}\beta_P(i)\right)^2}} \quad (32)$$

The next iteration of the procedure follows ... to the first ... . This process is continued until ... successive values of S_A and S_{new} differ negligibly. The final ... profile and S_A are then used to calculate the extinction profile, $\sigma_P(z)$. The σ_P profile is given

$$\sigma_P(z) = S_P\beta_P(z) \quad (33)$$

and the uncertainty in $\sigma_P(z)$ is

14

$$\delta\sigma_P(z) = \sigma_P(z)\sqrt{\left[\frac{\delta S_A}{S_A}\right]^2 + \left[\frac{\delta\beta_P(z)}{\beta_P(z)}\right]^2} \qquad (34)$$

The σ_P profile is then numerically integrated from the ground to the aerosol top height to produce an AOD profile, $\tau_P(z)$.

$$\tau_P(z) = \int_{z_L}^{z^*} \sigma_P(z')dz' \qquad (35)$$

and the uncertainty in $\tau_P(z)$ is

$$\delta\tau_P(z) = (\Delta z)^2 \sum_{i=z_L}^{z^*} (\delta\sigma_P(i))^2 \qquad (36)$$

The final data products from the inversion procedure are S_A, and profiles of aerosol backscatter, extinction, and optical depth.

4.3 Level 2 Data Products

Level 2 data are not available in real-time but are quality assured products. Level 2 data use the same algorithm described in the previous section, but level 2 AOD from AERONET instead of 1.5 AOD. Level 2 MPLNET data are available only after AERONET completes their level 2 processing. To produce Level 2 data, a month-long section of Level 1.5 MPLNET data is screened to remove bad data using four criteria: instrument temperature, standard deviation of calibration values from the month-long average, χ_m values for each data point, and the fraction of clouds present during each calibration. The surviving data are manually inspected for one final check before completing the Level 2 process.

Preliminary laboratory investigations indicate a non-trivial temperature sensitivity among the MPL components (unpublished data). Temperature chamber tests have shown that the optical alignment (i.e., spot size, bore sight, etc) becomes noticeably different after temperature changes between 2° to 5° Celsius. Therefore, the initial MPL assembly, overlap calibrations, and data acquisition must all be done within ~5°C temperature range of each other to obtain accurate results. The target temperature is recorded during MPL assembly, and is referred to as the calibration temperature (often unique to each MPL). Normal on-site MPL operating temperatures occasionally lie outside an acceptable range from the calibration temperature due to power failures, operator error, and related causes. Level 1.5 data that lie outside the acceptable calibration temperature range are removed.

The individual C values are compared to their monthly average. The MPL calibration value will not change noticeably over one month unless an instrument problem occurs. Therefore, outlier C values are most likely due to bad data caused by cirrus cloud contamination in the AERONET AOD, low clouds in the NRB signals that were missed during the level 1.5 cloud screen, difference in AOD between the view angles of the MPL and sunphotometer, and/or NRB signals with high uncertainties. Level 1.5 data with C values greater than a 5% deviation from the monthly average are removed. Due to statistical fluctuations, it is possible to have data with high NRB uncertainties that adversely affect other data products, but C values that are close

to the monthly average. A simple check for outlying C values will miss such cases. Therefore, the χ_m parameter is inspected for the remaining data. If χ_m surpasses a certain threshold (typically between 1.1 and 1.2), then the data are removed.

Finally, the number of cloud-free signals during the initial 1.5 signal average is used to calculate the cloud-free fraction for each data point. If only a small portion of the signals during a 20 to 30 minute average were used to obtain 1.5 data, then the results are not representative of the time period and may be contaminated by clouds despite the screening procedures above. Level 1.5 data with low cloud-free signal fractions (typically < 0.5) are removed.

4.4 Level 3 Data Products

Level 3 data provide continuous, day and night, retrievals of aerosol heights and optical properties. The level 3 data are not available in real-time, but are quality assured. The level 3 algorithm uses a calibration function obtained by fitting values of C from the level 2 data. A polynomial fit is applied to the C values in order to allow for variations caused by changes in the window quality throughout the data period.

Once the calibration function is determined, a modified version of the level 2 algorithm is used to determine aerosol extinction profiles continuously throughout the month. The data are no longer tied to AERONET observations because the MPL is already calibrated. The AOD can be calculated from the level 1 data directly using the following procedure. First, the 1.5 cloud screen is used to remove cloudy signals. The Level 2 temperature screen is used to remove signals outside the acceptable calibration temperature range.

The signals that pass the initial screens are then averaged over a period of 20 minutes. A running calibration zone is then generated. Interpolating between the Level 2 aerosol top heights forms a baseline zone bottom. The zone is then manually inspected to insure it is free of clouds and aerosols. If a suitable calibration zone cannot be obtained for any portion of the data set, that portion is not processed. The AOD is then calculated directly from the level 1 data in the calibration zone using

$$\tau_P = \frac{1}{2}\left(\ln\left[\int_{r_1}^{r_2}\beta_M(r')T_M^{2}(r')dr'\right] - \ln\left[\int_{r_1}^{r_2}P_{AB}(r')dr'\right]\right) \qquad (37)$$

where r_1 and r_2 are the bottom and top of the zone, respectively. The optical depth uncertainty is given by

$$\delta\tau_P = \frac{1}{2}\sqrt{\frac{(\Delta r)^2 \sum_{b=r_1}^{r_2}\left[\delta\left(\beta_M(r_b)T_M^{2}(r_b)\right)\right]^2}{\left[\int_{r_1}^{r_2}\beta_M(r')T_M^{2}(r')dr'\right]^2} + \frac{(\Delta r)^2\sum_{b=r_1}^{r_2}\left(\delta P_{AB}(r_b)\right)^2}{\left(\int_{r_1}^{r_2}P_{AB}(r')dr'\right)^2}} \qquad (38)$$

Once the AOD has been determined, S_A, and a profile of aerosol extinction is generated using the same algorithm for Level 1.5 data except that the constraining AOD was measured using the MPL and not the co-located sunphotometer. Level 3 data have inherently greater uncertainty than Level 1 and 2.

5. Discussion

In this section we present examples of data generated using the algorithms described in the previous section. Results from the GSFC site during May 1 to 4, 2001 are shown. Bias errors resulting from overlap correction and use of a constant extinction-to-backscatter ratio, the two primary sources of uncertainty, are also discussed.

5.1 Examples of MPLNET Data Products

Level 1 data are archived in daily increments and provide a qualitative representation of the overall structure of aerosol and cloud layers over the course of the day. Level 1 data from GSFC on May 2, 2001 are displayed in Figure 2. The top plate (a) shows the NRB signals from the ground to 20 km (asl) as a function of the fractional time of the day of the year (UTC). The Level 1 data are displayed at a resolution of 1-minute. The bottom plate (b) shows the percent uncertainty in Level 1 data at this time resolution. Sunrise occurs at about 1045 UTC (approximately 122.45 in fractional day of year) and is accompanied by increasing uncertainty in the NRB caused by rising solar background values (see the speckled appearance in the upper atmosphere after this time). In plate (a), molecular signals are the weakest and higher values of NRB indicate the presence of aerosols and clouds. Cloud layers typically have higher values than aerosols, and thus often appear very red to white in this type of plot, aerosols usually range from light blue to yellow in color, and signals from particle-free regions (molecules) usually appear purple to dark blue. The results show that aerosols are confined to within 6 km of the surface and that a cloud layer was intermittently present at an altitude near 10 km. Boundary layer clouds were present during the afternoon (near 122.8 in fractional day of year) at an altitude of 2 km. In addition to the identification of gross features, finer structure such as the evolution of the boundary layer aerosols is visible. The altitude of the nocturnal boundary layer was approximately 2 km, decreasing to near 1 km by sunrise. Some elevated aerosols were over the boundary layer, extending to an altitude of 6 km. By mid-morning (near 122.6 in fractional day of year), the boundary layer began to form a much more pronounced structure and top. The top of the boundary layer continued to rise, reaching a peak again near 2 km by the afternoon. Features such as the diurnal variation in aerosol vertical distribution are frequently observed at MPLNET sites.

Figure 3 shows an example of Level 1.5 data using signals acquired at GSFC at 1157 UTC on May 2, 2001, the same time as the AERONET observation. The NRB signals were averaged for 20-minutes, centered at 1157 UTC. Figure 3 shows the retrieved extinction profile with the gray bars representing the uncertainty in the extinction values at each altitude bin. The magnitude of the extinction uncertainties should not be considered representative of all MPLNET data because the degree of uncertainty depends upon factors that are different for each MPL system and measurement condition (just as the extinction profile itself is always different). We show this profile merely as a fairly typical example of data acquired at GSFC during the May 1 to 4, 2001 period. Other Level 1.5 data products such as C, S_A, and the aerosol top height are shown in the text box, along with some of the AERONET data. While the aerosol top height is fairly high (> 5 km) the majority of the aerosols are confined to the boundary layer (< 2 km) and this distribution is fairly common at GSFC during that time of year. The S_A value is high and

17

---

in the range of values observed for continental pollution (Anderson et al. 2000; Ferrare et al. 2001; Welton et al. 2002).

Examples of Level 3 data products are shown in Figure 4. NRB signals at GSFC from May 1, 2001 to May 4, 2001 are shown in the top plot (a). The evolutions of aerosol distributions in the boundary layer and above, to a height of about 6 km, over the four-day period are shown. The speckled appearance in the NRB signals at high altitudes marks the daytime portions during each day. The diurnal cycle in the growth and decay of the boundary layer is clearly evident when plotted as a multi-day image. Aerosol signal returns are shown to increase above the boundary layer as time progresses towards May 4. Some high clouds are also shown from 8 to 12 km. Very high signal levels near the surface at the end of May 1 were not caused by the atmosphere, but instead to a failure in the air conditioning system for the room housing the MPL at GSFC. The temperature rose to near 40°C and caused the optical alignment of the MPL to shift, thereby corrupting the data. This period of time was screened out of further analysis. Plot (b) shows the Level 2 C values obtained during this four-day period. For the Level 3 calculations in this example, the value of C was assumed to be constant and equal to 200 $(km^3 \cdot sr)/(\mu J \cdot \mu sec)$ instead of using a more sophisticated higher order polynomial fit. The fixed value is a good representation for May 1 to May 3, but overestimates C on May 4. Use of the fixed C value on May 4 is used here to illustrate the impact of incorrectly estimating C. Profiles of backscatter and extinction, and the optical depth and extinction-to-backscatter ratio for each layer were calculated using the fixed value of C and the Level 3 algorithm. Plot (c) displays the calculated aerosol extinction profiles during the four-day period. The structure of the aerosols are more visible here than in the Level 1 data. The cloud and temperature screens were employed to remove periods contaminated by clouds and the bad data near the time of the air conditioning failure. Occasional periods with high NRB or extinction profile uncertainties have been screened as well. It is possible to quantify how much aerosol data is lost due to the various data screens. In this example the algorithm was able to process over 75% of the aerosol data. Plot (d) shows a comparison between the AERONET Level 2 AOD and the MPLNET Level 3 AOD calculated using the fixed C value. The two data should agree during periods when the AERONET sunphotometer was operating because the MPL calibration value is tied to the AERONET AOD. There is good agreement between the two, except for May 4. On this day, the MPL systematically overestimates the AERONET AOD because the fixed value of C was larger than the real values calculated from Level 2 processing. This also implies that the retrieved extinction profiles on May 4 are two high in magnitude. The May 4 case presents the implications of performing a poor fit to the calibration data. Plot (d) also shows the ability of the Level 3 algorithm to calculate optical depth during both the day and night. This capability can significantly extend the data already collected at AERONET sites, which at this time are limited to only daytime operation.

5.2 Bias Errors in MPLNET Data Products

The algorithms presented in Section 4 utilize propagation of error techniques to quantify uncertainties in MPLNET data. However, it is not possible to quantify all sources of proposed error. Human error during the correction of Level 0 data and assumptions, such as the use of a constant extinction-to-backscatter ratio, are sources of possible bias error and can not be directly quantified.

18

5.2.1 Overlap Correction Bias and Extinction-to-backscatter Ratio Assumptions

As discussed in Section 4.1, Level 0 data must be corrected for effects caused by instrument parameters. The largest impact on the resulting Level 1 data is due to the overlap correction, which corrects signals in the near field for losses due to the MPL overlap function. The overlap correction procedure does require some degree of human subjectivity, the other corrections do not. As described in Campbell et al. (2002), the overlap function is derived by performing measurements with the MPL oriented horizontally. A plot of the natural logarithm of the signal versus range should produce a linear function if the atmosphere is horizontally homogeneous along the observation path. A linear fit to the data in the far field is performed, and the fit is extrapolated through to the near field. The fit is used to solve for the overlap function using data in the near field, and an assumption of horizontal homogeneity. The overlap correction algorithm accounts for all uncertainties derived from the measured quantities used to determine the overlap function. However, it is not possible to account for a poor fit or a fit to data that was taken during conditions not suited to overlap measurements (human errors).

Errors from using an assumption of range constant extinction-to-backscatter ratios in analysis of MPL data are discussed in Welton (1998) and Welton et al. (2000), and are also well documented in many journal articles in relation to analysis of data from any elastic backscatter lidar. The retrieved extinction profile is most sensitive to this source of possible error. The MPLNET algorithms use a predetermined optical depth measurement as a constraint to solve for extinction (and the layer-averaged extinction-to-backscatter ratio), therefore the final extinction profile will integrate to the correct optical depth. However the extinction value at any given altitude may be underestimated or overestimated based on the degree of difference between the calculated layer-averaged extinction-to-backscatter ratio and the actual value at that altitude. Since the height dependence of the extinction-to-backscatter ratio is not known, it is not possible to directly quantify any error due to this effect. Despite this problem, the range-constant algorithm is used to process MPLNET data because it is easy to implement. Also, the procedure calculates an average extinction-to-backscatter ratio, which is more accurate than simply guessing a value to use or assuming some range dependence based on a model. The latter would cause the data to be biased to the model used in the inversion. Furthermore, an average extinction-to-backscatter ratio does have value on its own since it is inversely proportional to the phase function and single scatter albedo, two quantities often measured as column averages. A lidar is the only instrument capable of measuring the phase function value exactly at 180° scattering angle.

Techniques other than propagation of errors are used to assess the degree of uncertainty introduced by these bias errors. Level 1 MPLNET data are routinely examined to see if a noticeable bias has been introduced as a result of poor overlap correction. First, the signals in the near field are examined to see if they fall below the limit expected for a theoretically modeled molecular lidar signal. Signals near the surface are also examined to see if they suddenly increase unexpectedly towards levels higher approaching those measured within clouds. Multi-day plots of Level 1 data are used to check for unnatural features near the surface, such as consistently low or high signal levels that always start and end at the same altitude bins. If present, all of these effects indicate that a poor overlap correction was used to generate the data. As a final check, results from initial Level 1.5 data are inspected. Poor overlap corrections typically result in unrealistic calculations of S_A (either very low or high), and extinction profiles that do not appear to adequately represent the structure seen in the Level 1 data. In terms of investigating the impact

---

of using constant extinction-to-backscatter ratios, Welton et al. (2002) have studied MPL results in order to attempt to discover meteorological conditions that introduce the highest degree of uncertainty. The results showed that when the atmosphere was composed of one dominant aerosol type, the retrieved extinction profile was more accurate than when several aerosol types were present. Also, when more than one aerosol type was type was present and convective mixing throughout the lower atmosphere was allowed, the retrieved extinction profile was found to be more accurate than when strong temperature inversions were present and mixing was suppressed. Under strong convective mixing, it would be unlikely to find a large gradient in aerosol properties, such as S_A.

Recent studies of actual S_A vertical profile measurements have also been conducted. Ferrare et al. (2001) report that Raman lidar results from the ARM Oklahoma site show that variations greater than 15% in the vertical profile of S_A occur only about 30% of the time. Therefore, most of the time the percent variation of the S_A vertical profile over Oklahoma varies less than the average calculated MPLNET S_A uncertainty at GSFC (approximately 20%), a site with similar aerosol as the ARM location. For these types of conditions, the actual variation in the S_A profile would have a negligible effect on the resulting MPLNET derived extinction profile. In addition, Masonis (2001) presents measurements of S_A during INDOEX using a 180° backscatter nephelometer. Averages of S_A obtained throughout the campaign yielded values of 51.4 sr below 750 m, 65.7 sr between 750 and 1500 m, and 73.1 sr above 1500 m. These results show a mean vertical variation of approximately 17% from the surface to the free-troposphere, which is also within typical MPLNET uncertainties for S_A.

Based on these findings, many of the observation conditions at MPLNET sites would be expected to produce results that are somewhat insensitive to vertical variations in S_A. However, unless the meteorological conditions are known a priori and a guess as to vertical variation of S_A can be made, this possible source of bias error must be considered when analyzing MPLNET results. It is important to consider that the lower atmosphere S_A values often contain more variation than those in the free-troposphere (Masonis 2001). Therefore, it is expected that the portion of the MPLNET derived extinction profile in the boundary layer would contain higher possible bias error than the portion above.

5.2.2 Extinction Comparisons with Other Instruments

The best method of determining the degree of bias introduced by the overlap correction and constant extinction-to-backscatter ratio assumption is to compare MPLNET extinction data to those obtained from other instruments. Comparisons between MPL data and other independent extinction measurements have been completed during five past field experiments: ACE-2, INDOEX, PRIDE, SAFARI-2000, and ACE-Asia. ACE-2 and INDOEX both pre-date MPLNET, however the algorithm used to retrieve the extinction profile uses the same AOD constraint technique as the one discussed in Section 4. In addition, overlap corrections were necessary in each experiment. The results of each comparison are discussed in greater detail in the corresponding reference listed below, a summary is provided here. The comparisons during ACE-2, PRIDE, SAFARI-2000, and ACE-Asia were made with the NASA Ames Airborne Tracking Sunphotometer (AATS) (Schmid et al. 2000; Livingston et al. 2003; Schmid et al. 2003a; Schmid et al. 2003b). The AATS acquires profiles of AOD, at or within a few nanometers of the MPL wavelength, by spiraling over the lidar site from very near the surface to a maximum altitude of approximately 5 km. The AOD is differentiated to produce extinction

profiles. The comparisons during INDOEX were made with calculated surface extinction values generated using data from co-located nephelometers and absorption photometers operated by the Climate Chemistry Group at NOAA Pacific Marine Environmental Laboratory (Quinn et al. 2002).

During ACE-2, comparisons of AOD profiles through a layer of Saharan dust were made using an MPL and the AATS-6 (Welton et al. 2000). The MPL AOD profile was generated by integrating the extinction profile. Results showed that the profile of AOD from the MPL agreed with the AATS-6 AOD profile within 6% (the uncertainty in the MPL data) throughout the layer.

MPL data from the research ship platform in INDOEX were partitioned into categories according to the origins of air masses, and corresponding temperature and humidity profiles, that were encountered at different times during the research cruise (see Figures 9 and 10 in Welton et al. 2002]. The average MPL derived extinction value near the surface was calculated for each category and compared with extinction values calculated on the ship using NOAA nephelometers and absorption photometers. The difference in altitude between the MPL and NOAA derived extinction values was 56 meters. The MPL values overestimated extinction relative to the values measured on the ship. However, three of the categories agreed well when the uncertainties in both the MPL and NOAA derived extinctions were taken into account. The comparisons showed that the categories closest to a 1:1 correlation were those having fairly weak marine boundary layer (MBL) inversions. These categories included clean marine regions as well as those impacted by continental pollution that originated over the Indian sub-continent. The remaining two categories with the poor agreement contained strong inversions at the top of the MBL with surface trajectories originating over the northern Indian Ocean and air masses above the MBL that originated over land. The authors also report that successful overlap measurements were not possible for another MPL site in INDOEX. Therefore they did not process data products at that site that were dependent upon correcting overlap losses. This indicates that successful overlap measurements are not always possible, but that poor overlap calculations derived from bad measurements can be screened out.

Four comparisons between an MPL and the AATS-6 were analyzed (Livingston et al. 2003) during PRIDE. The MPL site was situated on the eastern coast of Puerto Rico, and was influenced by sea salt, Saharan dust, and pollution aerosols (locally produced on the island). In all cases, Saharan dust was present above the marine boundary layer, MBL (~ 1.5 km). The 1.5 km. Good agreement is defined as having the AATS-6 derived extinction profiles above the uncertainty in the MPL profile, which for this work also included the spread in the MPL data caused by changes in the atmosphere over the time period of the comparison. Extinction comparisons at altitudes near the top of the MBL showed poor agreement. However, in three out of the four cases good agreement was found for extinction comparisons within 500 m of the surface. The one case with poor agreement from the surface to the top of the MBL occurred on a day with a very sharp inversion at 1.5 km (see Figure 6 in Livingston et al. 2003). As reported by Welton et al. (2002), the algorithm often fails to determine correct extinction values when mixing between the MBL and air above was inhibited by a strong temperature inversion. Examination of the results from the other days showed that no overlap bias was apparent because the extinction comparisons were good near the surface (where the overlap correction is largest), and throughout the rest of the profile except near the top of the MBL. Disagreement near the top of the MBL could have been due to the fact that the AATS-6 extinction is calculated from column measurements of AOD and numerical smoothing of the profile prior to differentiation.

The MPL is more sensitive to discreet changes in aerosol backscatter at individual altitudes than the AATS-6. Livingston et al. also show profiles from a Forward Scattering Spectrometer Probe (FSSP) optical particle counter, co-located with AATS-6, for the four comparisons. Peaks in the FSSP profile near the top of the MBL are present in each comparison. The FSSP data indicate that the sharp peak in MPL derived extinction at the MBL top was likely caused by a sudden change in either particle concentration or size (perhaps caused by particle swelling in the high humidity near the MBL top).

Schmid et al. (2003) present a comparison between the MPL and the AATS-14 during SAFARI-2000 (see Figure 8). The comparison was performed in a region dominated by pollution generated in Southern Africa and smoke from biomass burning in the area. The authors report that the MPL and AATS-14 derived extinction values are remarkably similar above 1 km (the altitude of the boundary layer), but show much worse agreement below that altitude (similar to PRIDE). However, the extinction values derived from both instruments agree within the net uncertainty in the MPL profile at all altitudes. The net uncertainty in the MPL data was not shown in the figure, but averaged about 50% throughout the whole profile. The net uncertainty included variations over the time period of the overflight (approximately 1 hour), as well as the quantified uncertainties calculated by the MPLNET algorithm. McGill et al. (2003) discuss the effects of time averaging ground-based MPL data for comparisons to airborne instruments, in their case the NASA Cloud Physics Lidar (CPL). The CPL was included in the Schmid et al. comparison, and also shows good agreement with the MPL and AATS-14 above 1 km, but worse comparisons between all three instruments below that altitude. McGill et al. report that a likely cause of disagreement between the three instruments below 1 km was due to differences in time averages and geographic location between each platform. Over periods of ~ 1 hour, changes in aerosol concentration and optical properties are much more likely to occur in the boundary layer then higher in the troposphere due to the greater instability of the boundary layer. In addition, smoke plumes are not homogeneous in space and time, and can cause large fluctuations in the boundary layer (where much of the smoke is confined). In fact, inspection of MPL derived extinction profiles approximately 1 hour earlier than the overflight of the CPL agreed very well with the CPL profile below 1 km.

6. Conclusion

The organization of a standardized global ground-based lidar network, MPLNET, has been presented. The micro-pulse lidar was selected as the network instrument because it is eye-safe, compact, and commercially available, allowing growth within the network while maintaining standardized instrumentation. The main objective of MPLNET was to co-locate MPL systems with sunphotometers at AERONET sites located in unique aerosol and geographic regions.

The MPLNET sites acquire aerosol vertical profiles in addition to the column-averaged properties available from AERONET, and provide both day and nighttime data. Operational protocols and data analysis techniques have been developed to process MPLNET data. Uncertainty calculations account for all known sources of potential error, and the results show that successful aerosol extinction retrievals are possible. Bias errors that cannot be accounted for have been presented. The primary bias error arises from assumption of a constant S_A throughout the aerosol layer. This problem is inherent to the backscatter-lidar-sunphotometer retrieval

technique, and cannot be overcome. However, many comparisons between MPL extinction profiles and independent measurements of extinction show that on average the MPL retrievals agree well in shape and magnitude with results from the other techniques. As a result, vertical changes in S_a, on average, may be less significant than other sources of uncertainty that are accounted for in the retrieval. For those atmospheric situations that would create the largest bias error, trends have been identified and include strongly stratified adjacent aerosol layers.

Improvements to the MPL telescope are also underway. A co-aligned mini-receiver attachment for the MPL design has been designed. The mini-receiver has a much larger field-of-view than the MPL receiver, and will record return signals in real-time. In theory, the MPL overlap function can be calculated from a ratio of the two signals. This process may allow the MPL overlap to be determined using the operational data, negating the need to perform a separate series of often difficult horizontal measurements. Improvements to the MPL transmit path are also being considered. A replaceable laser source is being tested to determine if laser repair can be accomplished in the field without the need for re-alignment and re-calibration at NASA GSFC. The MPL detector has already been successfully fiber coupled, allowing similar removal without re-alignment of the receive optics.

New data products for MPLNET are also under development. These include real-time Level 1.5 cloud heights, and the addition of cloud layers in the Level 3 product. The new cloud height algorithm will be based on Campbell et al. (1998), but utilize MPLNET Level 1 signal uncertainties to help identify tenuous clouds in noisy data and reduce the number of false positives. Finally, the creation of merged multi-data product sets including MPLNET, AERONET, MODIS imagery, back-trajectories, and aerosol transport models has just begun. The merged data sets will lead to the creation of new more complex data products.

Appendix A

A.1 Molecular and Ozone Terms

Molecular backscatter profiles, $\beta_M(r)$, are generated using the tropical, mid-latitude winter, mid-latitude summer, arctic winter, and arctic summer models in the US Standard Atmospheres, 1976. Rayleigh scattering calculations for each model are given by (McClatchey et al. 1972). Molecular extinction values are calculated directly from the backscatter data using the Rayleigh extinction-to-backscatter ratio ($8\pi/3$, a constant). Tropical profiles are used from 0° to 30° latitude, mid-latitude profiles from 30° to 60°, and arctic from 60° to 90°. Summer seasons include April to September, and winter seasons the remaining months.

Ozone transmission profiles, $T_o^2(r)$, are determined using ozone mass mixing ratio profiles from a climatology developed at NASA Goddard Space Flight Center (G. Labow, unpublished data). The ozone climatology is segmented into discrete 10° latitude zones from the South to North Pole. The ozone mass mixing ratio profiles, $r_o(z)$, are converted to column density per kilometer (atm-cm/km), $\varepsilon_o(r)$, using the following equation,

$$\varepsilon_o(r) = \frac{r_o(r)\rho(r)}{2.14148\times10^{-5}}$$ (A.1)

where r is the altitude in km, and $\rho(z)$ is the atmospheric density at r (obtained using the US Standard Atmospheres models). The next step is to calculate the ozone transmission profiles. $T_o^2(r)$ is calculated using the following equation,

$$T_o^2(r) = \exp\left[-2\bullet c_o(\lambda)\int_{MPL-Altitude}^{r}\varepsilon_o(r')\,dr'\right]$$ (A.2)

where $c_o(\lambda)$ is the Chappius ozone absorption coefficient in cm^{-1}. The ozone absorption coefficient is generated at the MPL wavelength from a table compiled in Iqbal (1984) using data from Leckner (1978) and Vigroux (1953).

In order to assess the magnitude of the uncertainties in the molecular terms in Eq. (8), a model backscatter profile was calculated by averaging the tropical and arctic winter standard profiles. Maximum possible uncertainties for the molecular terms were estimated using the deviations of the two extreme standard atmospheres from the average model. The magnitude of the ozone uncertainty term was estimated by averaging together summer-tropical (0°-10° N latitude) and winter-polar (80°-90° S latitude) ozone profiles. Maximum uncertainties for the ozone term in Eq. (8) were determined in the same fashion as for the molecular terms, but using the average ozone profile. Figure 5 shows plots of the molecular and ozone uncertainty terms for ground-based vertically oriented viewing angles. The minimum uncertainty in molecular backscatter is the dominant term. The minimum uncertainty due to the combined molecular and ozone terms is found between 5 to 10 km. MPLNET calibration zones are usually located in this altitude range, therefore MPL calibrations can often be performed quite accurately. Ozone only becomes significant above 20 km. At the moment, there are no MPLNET stratospheric data products, therefore ozone terms are ignored in the current algorithms.

Based on these results, the estimated maximum uncertainty due to combined molecular and ozone parameters is about 2% from 5 to 10 km, and about 5% elsewhere (below 20 km). The models used above were constructed to produce maximum possible uncertainties. In actual situations, the molecular and ozone terms are determined more accurately than the model, because arctic profiles would not be used to analyze data taken near the equator. Therefore, actual uncertainties are even less then the maximum values reported here.

The sensitivity study was performed again, but with a more realistic assessment of fluctuations in the molecular and ozone profiles. The new study used mid-latitude summer and winter profiles to assess the degree of uncertainty in the molecular and ozone terms. The uncertainties were much lower, and averaged approximately 2% over the whole profile. Therefore, the current MPLNET algorithms set the combined uncertainty due to molecular and ozone terms to 2%.

A.2 Uncertainty in the Scattering Ratio

The $\delta\chi(r)$ term in Eq. (8) is the uncertainty in the scattering ratio. If $\chi(r)$ were actually measured during the calibration process then $\delta\chi(r)$ would be determined from the uncertainty in the measurement. However, such measurements are not possible, therefore $\chi(r)$ is assumed to be 1. If during a calibration $\chi(r)$ is actually greater than 1 due to the presence of particles, then the NRB signal increases by a factor proportional to $\chi(r)$. In such a case, an incorrect, and high, value of C would be calculated because the denominator in Eq. (6) was not compensated for by the presence of particle backscatter. Therefore, an uncertainty exists due to the assumption of $\chi(r) = 1$ and is given by

$$\frac{\delta\chi(r)}{\chi(r)} = [\chi_m - 1]$$ (A.3)

where χ_m is the minimum scattering ratio detection limit.

Figure 6 illustrates the use of Eq. (14). A modeled NRB signal from a ground-based lidar was constructed using a boundary layer from 0 to 2 km, with $\beta_P = 0.001$ km⁻¹·sr⁻¹ and $\sigma_P = 0.025$ km⁻¹. C was set to 1 for this model. A candidate calibration zone was designated from 4 to 5 km, with varying values of $\chi(r)$: 1.00, 1.05, 1.10, and 1.20. The NRB signal uncertainty was set at 5%. Figure 1 shows plots of the NRB signal with no particles present in the calibration zone ($\chi(r)=1$), and with particles present ($\chi(r)>1$). As the particle concentration and $\chi(r)$ increase, it becomes easier to detect the presence of particles in the candidate calibration zone. Figure 1 shows that the presence of particles becomes masked by the signal noise when $\chi(r) \approx 1.05$ or less. Therefore, the value of χ_m is about 1.05 for this example. In general, the value of χ_m is dependent upon the NRB signal uncertainty in the calibration zone,

$$\chi_m = \left[\frac{\delta\bar{P}_{NRB}}{\bar{P}_{NRB}}\right] + 1$$ (A.4)

where $\bar{P}_{NRB}$ and $\delta\bar{P}_{NRB}$ are the average NRB signal and uncertainty in the calibration zone. The most accurate calibration values will be calculated when the NRB signal uncertainty is small.

A.3 Uncertainty in the Particle Transmission

The particle transmission term in the calibration zone is constant and equal to $\exp(-2\tau_P)$. The uncertainty in the T_P^2 term in Eq. (8) is due to the uncertainty in the aerosol optical depth, τ_P, between the MPL and the calibration zone. δT_P^2 is given by

$$\left[\frac{\delta T_P^2}{T_P^2}\right] = 2\delta\tau_P$$ (A.5)

where $\delta\tau_P$ is the uncertainty in the aerosol optical depth. AERONET reports an optical depth uncertainty usually on the order of ± 0.01. Actual reported values of $\delta\tau_P$ are used for MPLNET processing. During research cruise deployments, a co-located AERONET sunphotometer is not present, and the calibration is performed using optical depths calculated with a handheld Microtops Sunphotometer and the NASA SIMBIOS sunphotometer algorithm (Knobelspiesse et al. 2003). The uncertainty in the microtops derived uncertainty is typically about ± 0.02.

Acknowledgments

References

Ackermann, J., 1998: The extinction-to-backscatter ratio of tropospheric aerosol: A numerical study. *J. Atmos. Oceanic Technol.*, **15**, 1043-1050.

Anderson T. L., S. J. Masonis, D. S. Covert, R. J. Charlson, M. J. Rood, 2000: In situ measurement of the aerosol extinction-to-backscatter ratio at a polluted continental site. *J. Geophys. Res.*, **105**, 26907-26915.

Bösenberg, J., A. Ansmann, J. M. Baldasano, D. Balis, C. Böckmann, B. Calpini, A. Chaikovsky, P. Flamant, A. Hågård, V. Mitev, A. Papayannis, J. Pelon, D. Resendes, J. Schneider, N. Spinelli, T. Trickl, G. Vaughan, G. Visconti, M. Wiegner, 2001: EARLINET: A European Aerosol Research Lidar Network. Editions de l'Ecole polytechnique – Février, ISBN 2-7302-0798-8, 155-158.

Campbell, JR, DL Hlavka, JD Spinhirne, DD Turner, and CJ Flynn, 1998: Operational Cloud Boundary Detection and Analysis from Micro Pulse Lidar Data. In *Proceedings of the 8th ARM Science Team Meeting*, Ed. by N. Burleigh and D. Carrothers, U.S. Department of Energy, Richland, WA, 119-122.

Campbell, J.R., D.L. Hlavka, E.J. Welton, C.J. Flynn, D.D. Turner, J.D. Spinhirne, V.S. Scott, and I.H. Hwang, 2002: Full-time, Eye-Safe Cloud and Aerosol Lidar Observation at Atmospheric Radiation Measurement Program Sites: Instrument and Data Processing. *J. Atmos. Oceanic Technol.*, **19**, 431-442.

Campbell, J. R., E. J. Welton, J. D. Spinhirne, Q. Ji, S. Tsay, S. J. Piketh, M. Barenbrug, and B. N. Holben, 2003: Micropulse Lidar observations of tropospheric aerosols over northeastern South Africa during the ARREX and SAFARI-2000 Dry Season experiments. *J. Geophys. Res.*, **108**, 8497, doi:10.1029/2002JD002563.

Holben B.N., T.F.Eck, I.Slutsker, D.Tanre, J.P.Buis, A.Setzer, E.Vermote, J.A.Reagan, Y.Kaufman, T.Nakajima, F.Lavenu, I.Jankowiak, and A.Smirnov, 1998: AERONET - A federated instrument network and data archive for aerosol characterization. *Rem. Sens. Environ.*, **66**, 1-16.

Houghton, J.T., Y. Ding, D.J. Griggs, M. Noguer, P.J. van der Linden, X. Dai, K. Maskell, and C.A. Johnson (eds.), 2001: IPCC, 2001: Climate Change 2001: The Scientific Basis, Contribution of Working Group I to the Third Assessment Report of the Intergovernmental Panel on Climate Change. Cambridge University Press, Cambridge, United Kingdom and New York, NY, USA, 881pp.

Huebert, B. J., T. Bates, P. B. Russell, G. Shi, Y. J. Kim, K. Kawamura, G. Carmichael, and T. Nakajima, 2003: An overview of ACE-Asia: Strategies for quantifying the relationships between Asian aerosols and their climatic impacts. *J. Geophys. Res.*, **108**, 8633, doi:10.1029/2003JD003550.

Fernald, F. G., B. M. Herman, and J. A. Regan, 1972: Determination of Aerosol Height Distributions by Lidar. *J. Appl. Meteorol.*, **11**, 482-489.

Fernald, F. G., 1984: Analysis of atmospheric lidar observations: some comments. *Appl. Opt.*, **23**, 652-653.

Ferrare, R. A., D. D. Turner, L. H. Brasseur, W. F. Feltz, O. Dubovik, and T. P. Tooman, 2001: Raman lidar measurements of the aerosol extinction-to-backscatter ratio over the Southern Great Plains. *J. Geophys. Res.*, **106**, 20333-20347.

Herman, J. R., P. K. Bhartia, O. Torres, C. Hsu, C. Seftor, and E. Celarier, 1997: Global distribution of UV-absorbing aerosols from Nimbus-7/TOMS data. *J. Geophys. Res.*, **102**, 16911-16922.

Iqbal, M., 1983: An Introduction to Solar Radiation, Academic Press, New York, NY.

Leckner, B., 1978: Spectral Distribution of Solar-Radiation at Earths Surface – Elements of a Model. *Solar Energy*, **20**, 143-150.

Kaufman, Y.J., D. Tanre, and O. Boucher, 2002: A satellite view of aerosols in the climate system. *Nature*, **419**, 215-223.

King, M. D., W. P. Menzel, Y. J. Kaufman, D. Tanre, B.-C. Gao, S. Platnick, S. A. Ackerman, L. A. Remer, R. Pincus, and P. A. Hubanks, 2003: Cloud and aerosol properties, precipitable water, and profiles of temperature and water vapor from MODIS. *IEEE Trans. Geosci. Rem. Sens.*, **41**, 442-458.

Klett, J. D., 1981: Stable analytical inversion solution for processing lidar returns. *Appl. Optics*, **20**, 211-220.

Knobelspiesse, K.D., C. Pietras and G.S. Fargion, 2003: Sun-Pointing Error Correction for Sea Deployment of the Microtops II Handheld Sun Photometer. *J. Atmos. Ocean. Tech.*, **20**, 767-771.

Kummerow, C., J. Simpson, O. Thiele, W. Barnes, A. T. C. Chang, E. Stocker, R. F. Adler, A. Hou, R. Kakar, F. Wentz, P. Ashcroft, T. Kozu, Y. Hong, K. Okamoto, T. Iguchi, H. Kuroiwa, E. Im, Z. Haddad, G. Huffman, B. Ferrier, W. S. Olson, E. Zipser, E. A. Smith, T. T. Wilheit, G. North, T. Krishnamurti, and K. Nakamura, 2000: The status of the Tropical Rainfall Measuring Mission (TRMM) after two years in orbit. *J. Appl. Meteorol.*, **39**, 1965-1982.

Lavoué, D., C. Liousse, H. Cachier, B. J. Stocks, and J. G. Goldammer, 2000: Modeling of carbonaceous particles emitted by boreal and temperate wildfires atnorthern latitudes. *J. Geophys. Res.*, **105**, p. 26871-26890.

Livingston, J. M., P. B. Russell, J. S. Reid, J. Redemann, B. Schmid, D. A. Allen, O. Torres, R. C. Levy, L. A. Remer, B. N. Holben, A. Smirnov, O. Dubovik, E. J. Welton, J. R. Campbell, J. Wang, and S. A. Christopher, 2003: Airborne Sun photometer measurements of aerosol optical depth and columnar water vapor during the Puerto Rico Dust Experiment and comparison with land, aircraft, and satellite measurements. J. Geophys. Res, 108, 8588, doi:10.1029/2002JD002520.

McClatchey, R. A., R. W. Fenn, J. E. A. Selby, F. E. Volz, and J. S. Garing, 1972: Optical Properties of the Atmosphere (Third Edition). AFCRL-72-0497, Environ. Res. Pap., 411, 108 pp., Air Force Cambridge Res. Lab., Hanscom Air Force Base, Mass.

McGill, M. J., D. L. Hlavka, W. D. Hart, E. J. Welton, and J. R. Campbell, 2003: Airborne Lidar Measurements of Aerosol Optical Properties During SAFARI-2000. J. Geophys. Res, 108, 8493, doi:10.1029/2002JD002370.

Marenco, F., Santacesaria, V., Bais, A.F., Balis, D., di Sarra, A., Papayannis, A., and Zerefos, C., 1997: Optical properties of tropospheric aerosols determined by lidar and spectrophotometric measurements (Photochemical Activity and Solar Ultraviolet Radiation campaign). Appl. Opt., 36, 6875-6886.

Masonis, S. J., 2001: An empirical study of the lidar ratio and its variability, with implications for determining climate forcing by satellite-borne lidar. Ph.D. Dissertation, University of Washington, Seattle, WA, 1-259.

Murayama, T., N. Sugimoto, I. Matsui, Z. Liu, T. Sakai, T. Shibata, Y. Iwasaka, J.-G. Won, S.-C. Yoon, T. Li, J. Zhou, and H. Hu, 2001: Lidar Network Observation of Asian Dust. Editions de l'Ecole polytechnique – Février, ISBN 2-7302-0798-8, 169-172.

Pope, C. A., R. T. Burnett, M. J. Thun, E. E. Calle, D. Krewski, K. Ito, and G. D. Thurston, 2002: Lung cancer, cardiopulmonary mortality, and long-term exposure to fine particulate air pollution. JAMA, 287, 1132-1141.

Quinn, P. K., D. J. Coffman, T. S. Bates, T. L. Miller, J. E. Johnson, E. J. Welton, C. Neusüss, M. Miller, and P. Sheridan, 2002: Aerosol Optical Properties during INDOEX 1999: Means, Variability, and Controlling Factors. J. Geophys. Res., 107, 8020, doi:10.1029/2000JD000037.

Raes, F., T. Bates, F. McGovern, and M. V. Liedekerke, 2000: The 2nd Aerosol Characterization Experiment (ACE-2): general overview and main results, Tellus, 52B, 111-125.

Ramanathan, V., P. J. Crutzen, J. Lelieveld, A. P. Mitra, D. Althausen, J. Anderson. M. O. Andreae, W. Cantrell, G. R. Cass, C. E. Chung, A. D. Clarke, J. A. Coakley, W. D. Collins, W. C. Conant, F. Dulac, J. Heintzenberg, A. J. Heymsfield, B. Holben, S. Howell, J. Hudson, A. Jayaraman, J. T. Kiehl, T. N. Krishnamurti, D. Lubin, G. McFarquhar, T. Novakov, J. A. Ogren, I. A. Podgorny, K. Prather, K. Priestley, J. M. Prospero, P. K. Quinn, K. Rajeev, P. Rasch, S. Rupert, R. Sadourny, S. K. Satheesh, G. E. Shaw, P. Sheridan, and F. P. J. Valero, 2001: Indian Ocean Experiment: An integrated analysis of the climate forcing and effects of the great Indo-Asian haze. J. Geophys. Res., 106, 28371-28398.

Reid, J. S., J. E. Kinney, D. L. Westphal, B. N. Holben, E. J. Welton, Si-Chee Tsay, D. P. Eleuterio, J. R. Campbell, S. A. Christopher, P. R. Colarco, H. H. Jonsson, J. M. Livingston, H. B. Maring, M. L. Meier, P. Pilewskie, J. M. Prospero, E. A. Reid, L. A. Remer, P. B. Russell, D. L. Savoie, A. Smirnov, and D. Tanre, 2003: Analysis of measurements of Saharan dust by airborne and ground-based remote sensing methods during the Puerto Rico Dust Experiment (PRIDE). J. Geophys. Res, 108, 8586, doi:10.1029/2002JD002493.

Russell, P. B., P. V. Hobbs, and L. L. Stowe, 1999: Aerosol properties and radiative effects in the United States East Coast haze plume: An overview of the Tropospheric Aerosol Radiative Forcing Observational Experiment (TARFOX). J. Geophys. Res., 104, 2213-2222.

Schmid, B., J. M. Livingston, P. B. Russell, P. A. Durkee, H. H. Jonsson, D. R. Collins, R. C. Flagan, J. H. Seinfeld, S. Gassó, D. A. Hegg, E. Öström, K. J. Noone, E. J. Welton, K. J. Voss, H. R. Gordon, P. Formenti, and M. O. Andreae, 2000: Clear sky closure studies of lower tropospheric aerosol and water vapor during ACE-2 using airborne sunphotometer, airborne in-situ, space-borne, and ground-based measurements. Tellus, 52B, 567-592.

Schmid, B., J. Redemann, P. B. Russell, P. V. Hobbs, D. L. Hlavka, M. J. McGill, B. N. Holben, E. J. Welton, J. Campbell, O. Torres, R. A. Kahn, D. J. Diner, M. C. Heimlinger, D. A. Chu, C. Robles Gonzalez, and G. de Leeuw, 2003a: Coordinated airborne, spaceborne, and ground-based measurements of massive, thick, aerosol layers during the dry season in Southern Africa. J. Geophys. Res., 108, 8496, doi:10.1029/2002TD002297.

Schmid, B., D. A. Hegg, J. Wang, D. Bates, J. Redemann, P. B. Russell, J. M. Livingston, H. H. Jonsson, E. J. Welton, J. H. Seinfeld, R. C. Flagan, D. S. Covert, O. Dubovik, and A. Jefferson, 2003b: Column closure studies of lower tropospheric aerosol and water vapor during ACE-Asia using airborne sunphotometer, airborne in-situ and ship-based lidar measurements. J. Geophys. Res, 108, 8656, doi:10.1029/2002JD003361.

Spinhirne, J. D., J. A. Reagan, and B. M. Herman, 1980: Vertical Distribution of Aerosol Extinction Cross Section and Inference of Aerosol Imaginary Index in the Troposphere by Lidar Technique. J. Appl. Meteorol., 19, 426-438.

Spinhirne, J. D., J. Rall, and V. S. Scott, 1995: Compact eye-safe lidar systems. Rev. Laser Eng., 23, 26-32.

1 Stokes, G. M., and S. E. Schwartz, 1994: The Atmospheric Radiation Measurement (ARM)
2 Program: Programmatic Background and Design of the Cloud and Radiation Test Bed. *Bull.*
3 *Amer. Meteor. Soc.*, **75**, 1201-1221.

4
5 Vigroux, E., 1953: Contribution a l'etude experimentale de l'absorption de l'ozone. *Ann. Phys.*,
6 **8**, 709-761.

7 Voss, K.J., E.J. Welton, P.K. Quinn, J. Johnson, A. Thompson, and H. Gordon, 2001: Lidar
8 Measurements During Aerosols99. *J. Geophys. Res.*, **106**, 20821-20832.

9
10 Welton, E. J., 1998: Measurements of Aerosol Optical Properties over the Ocean Using
11 Sunphotometry and Lidar. Ph.D. Dissertation. University of Miami, Coral Gables, 150 pp.

12
13 Welton, E. J., K. J. Voss, H. R. Gordon, H. Maring, A. Smirnov, B. Holben, B. Schmid, J. M.
14 Livingston, P. B. Russell, P. A. Durkee, P. Formenti, and M. O. Andreae, 2000: Ground-based
15 Lidar Measurements of Aerosols During ACE-2: Instrument Description, Results, and
16 Comparisons with other Ground-based and Airborne Measurements. *Tellus*, **52B**, 635-650.

17
18
19 Welton, E. J., K. J. Voss, P. K. Quinn, J. R. Campbell, J. D. Spinhirne, H. R. Gordon, and J. E.
20 Johnson, 2002: Measurements of aerosol vertical profiles and optical properties during INDOEX
21 1999 using micro-pulse lidars. *J. Geophys. Res*, **107**, 8019, doi:10.1029/2000JD000038.

22 Welton, E. J., and J. R. Campbell, 2002: Micro-pulse Lidar Signals: Uncertainty Analysis. *J.*
23 *Atmos. Oceanic Technol.*, **19**, 2089-2094.

24
25
26 Winker, D. M., J. R. Pelon, and M. P. McCormick, 2002: The CALIPSO mission: spaceborne
27 lidar for observation of aerosols and clouds. in Lidar Remote Sensing for Industry and
28 Environmental Monitoring III, U. N. Singh, T. Itabe, Z. Liu, (eds.), *Proc. SPIE*, **4893**, 1-11.

29
30 Zwally, H.J., B. Schutz, W. Abdalati, J. Abshire, C. Bentley, A. Brenner, J. Bufton, J. Dezio, D.
31 Hancock, D. Harding, T. Herring, B. Minster, K. Quinn, S. Palm, J. Spinhirne, and R. Thomas,
32 2002: ICESat's laser measurements of polar ice, atmosphere, ocean, and land. *J. Geodyn.*, **34**,
33 405-445.
34
35
36
37

Figure Captions

1 Figure 1. MPLNET site, field experiment, and ship cruise locations.
2
3
4 Figure 2. Level 1 normalized relative backscatter (NRB) signals (a) and corresponding percent
5 uncertainties (b) are shown for May 2, 2001 at NASA Goddard Space Flight Center in Maryland,
6 USA. The data were acquired at one-minute and 75 m time and vertical resolutions, respectively.
7
8
9 Figure 3. Level 1.5 aerosol extinction profile at 11:57 UTC on May 2, 2001 at NASA Goddard
10 Space Flight Center in Maryland, USA.
11
12 Figure 4. Level 1 normalized relative backscatter (NRB) signals are shown for May 1 to May 4,
13 2001 at NASA Goddard Space Flight Center in Maryland, USA (a). Level 1.5 and Level 2 MPL
14 calibration values obtained during this period are shown in (b). Level 3 aerosol extinction
15 profiles from May 1 to May 4 are shown in (c). Level 1.5 AERONET aerosol optical depth
16 (AOD) and Level 3 MPLNET AOD are shown in (d).
17
18 Figure 5. Maximum expected uncertainties for modeled molecular backscatter (solid-black),
19 molecular transmission (solid-gray), and ozone transmission (dashed) are shown.
20
21 Figure 6. Modeled normalized relative backscatter (NRB) signals with a fixed uncertainty of
22 5%, and a scattering ratio χ(r) of 1.0 (no aerosol), are shown in (a), (b), and (c) as the solid-black
23 line. Similar modeled NRB signals with fixed uncertainty of 5%, but with an aerosol layer from
24 4 to 5 km, are shown in (a), (b), and (c) as the solid-gray line. χ(r) within the aerosol layer varies
25 from 1.05 (a), 1.10 (b), to 1.20 (c) but remains fixed at 1.0 elsewhere in the profile.
26

Figure 1

Legend:
- ● Current Site
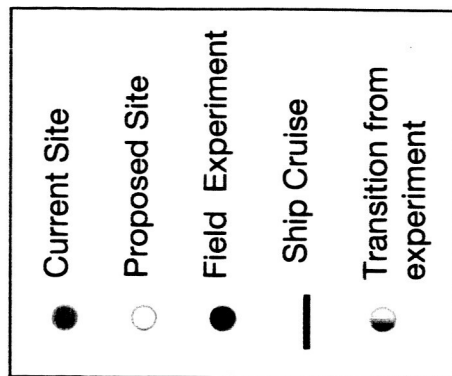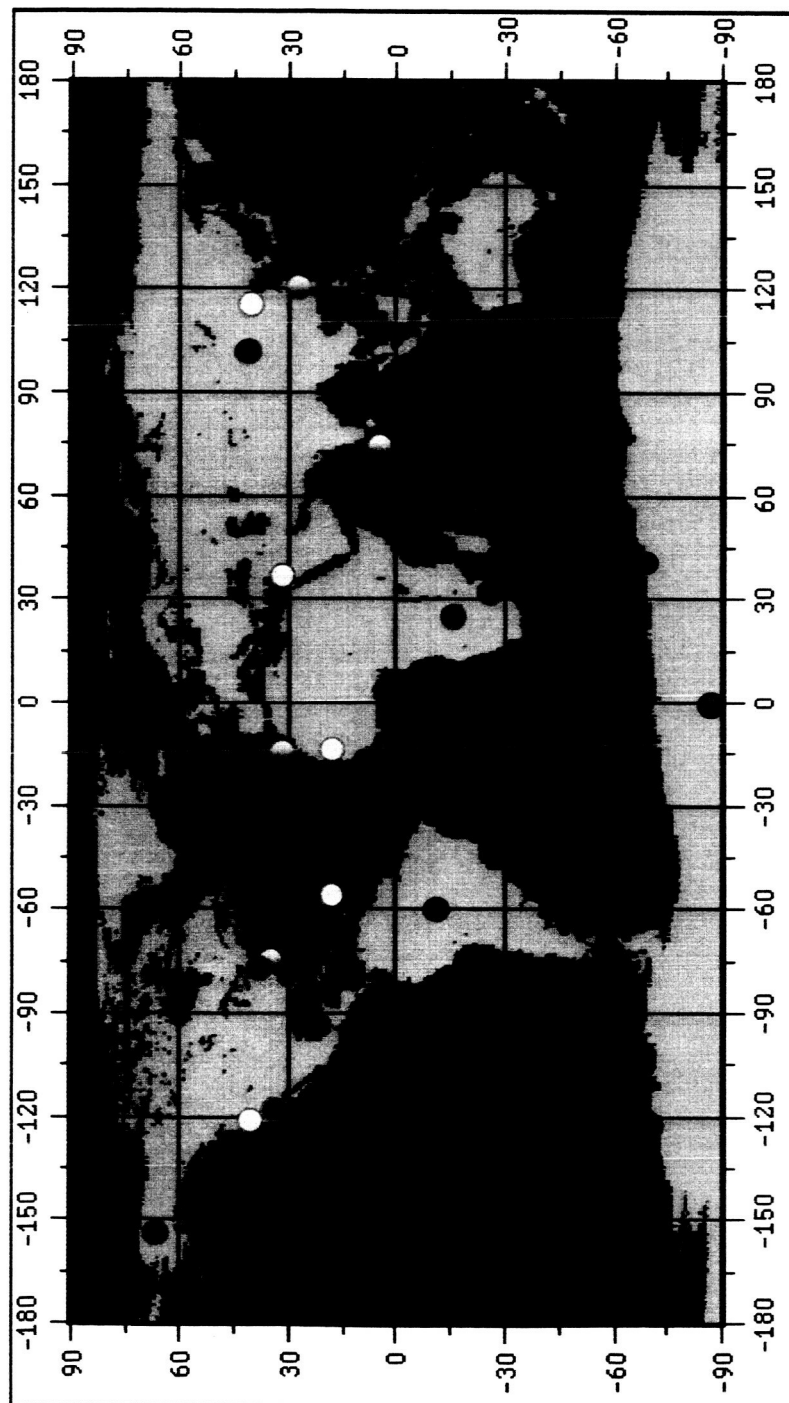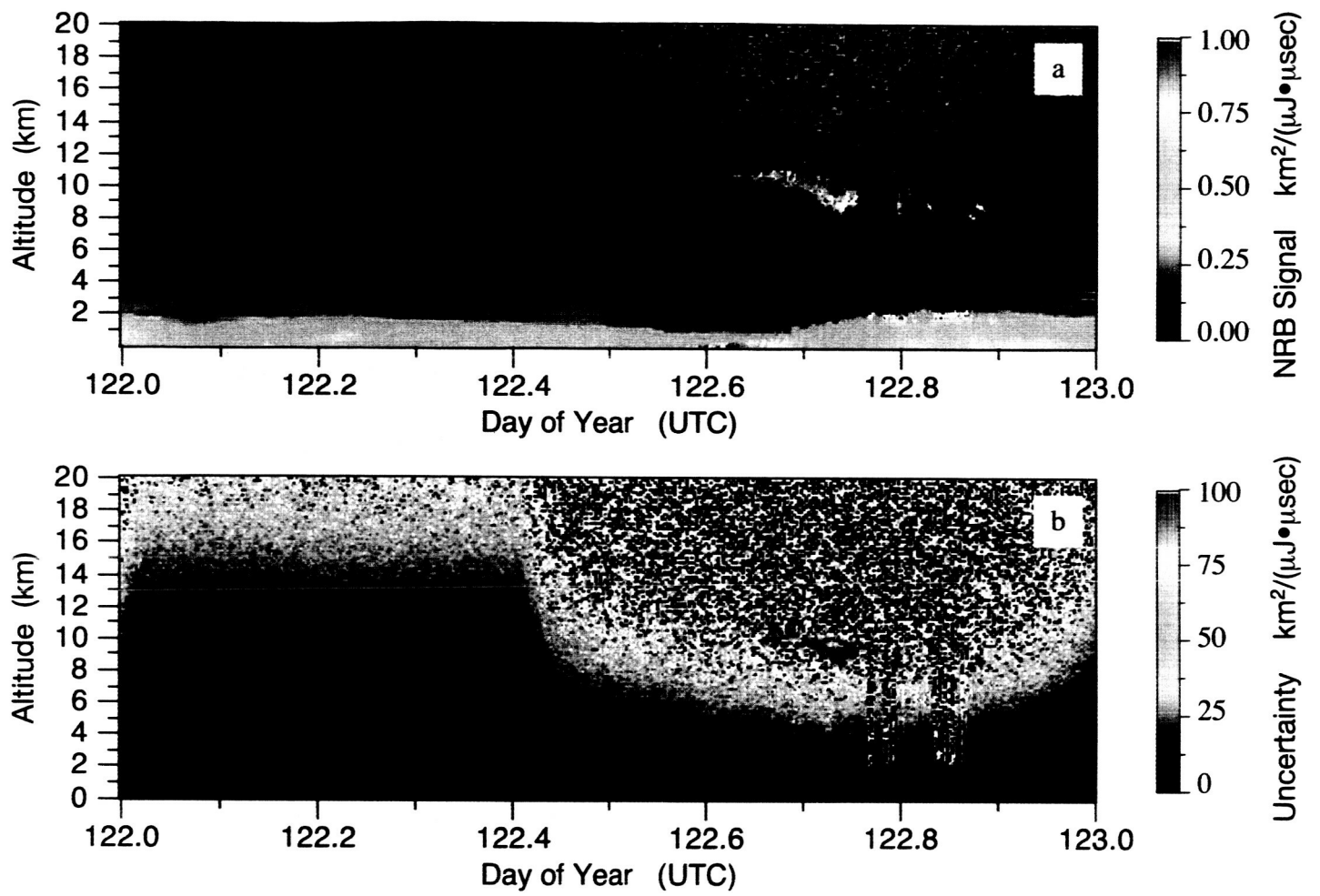- ○ Proposed Site
- ● Field Experiment
- — Ship Cruise
- ◑ Transition from experiment

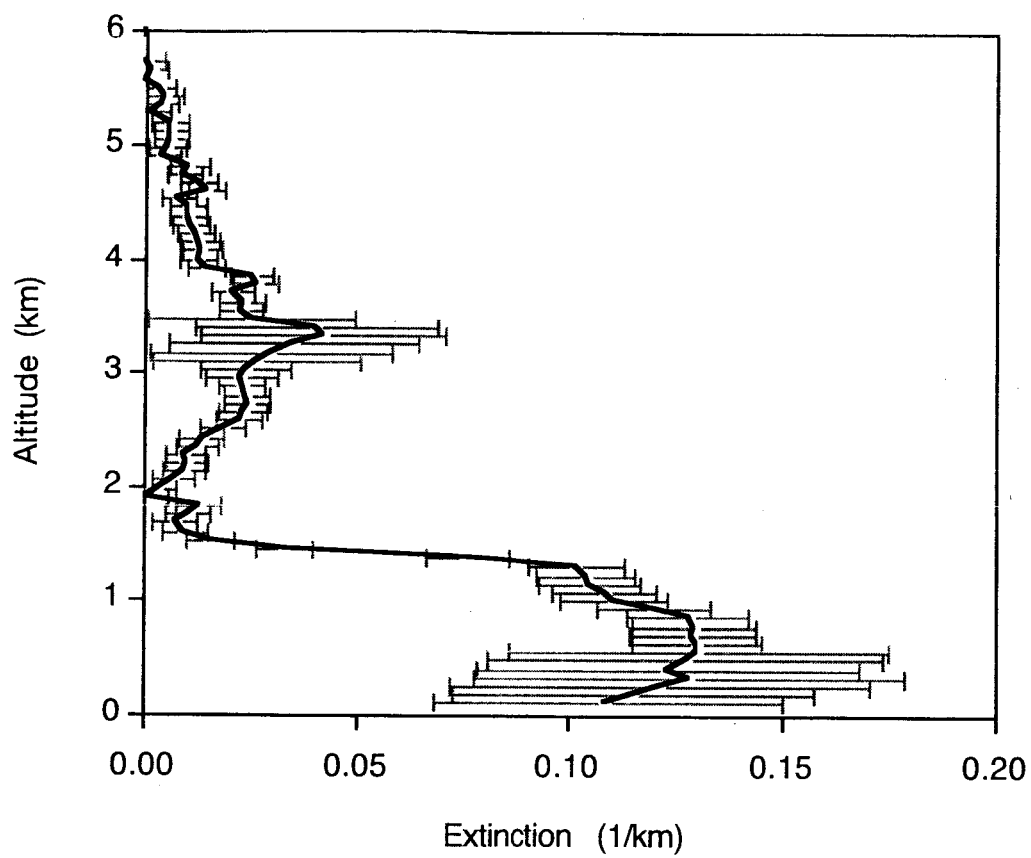Figure 2

Figure 3

Figure 4

Figure 5

Maximum Uncertainty (%)

Altitude (km)

Figure 6